Experimental Mechanics (2022) 62:837–847
https://doi.org/10.1007/s11340-022-00835-9

RESEARCH PAPER

Metal Artifacts in Attenuation and Phase Contrast X-Ray Microcomputed Tomography: A Comparative Study

J. Glinz[1,2] · S. Zabler[3,4] · J. Kastner[2] · S. Senck[2]

Received: 11 August 2021 / Accepted: 25 February 2022 / Published online: 17 March 2022

Abstract

Background Metal artifacts arising around high-density components are a widely known problem in X-ray computed tomography (XCT) for both medical and industrial applications. Although phase contrast imaging XCT (PCI-XCT) is known to be less prone to metal artifacts caused by beam hardening, so far only little effort was made for its comparison to other, more established methods.

Objective In the course of this work, this absence in literature is addressed by a quantitative comparison of PCI-XCT to attenuation contrast XCT (AC-XCT).

Methods A polymer specimen including four Ti6Al4V inserts was investigated by PCI- and AC-XCT with different pre-filter settings and metal artifact reduction (MAR) algorithm. Artifacts and image quality were evaluated by a streak index which provides a quantitative metric for the assessment of streak artifacts and contrast-to-noise ratio (CNR).

Results Results showed that streak artifacts are significantly reduced in PCI-XCT and only matched by AC-XCT in combination with hardware pre-filtering of the X-ray beam and post-processing by a MAR algorithm. However, hardware pre-filtering leads to worse CNR and artifacts close to the surface of metal inserts could not be removed sufficiently by the MAR algorithm.

Conclusions This work demonstrates the potential of PCI-XCT for the reduction of metal artifacts and presents the first quantitative comparison to established AC-XCT methods.

Keywords Metal artifacts · Beam hardening · Phase contrast imaging · X-ray microcomputed tomography

Introduction

In the past decades, X-ray microcomputed tomography (XCT) was established as an invaluable method for the three-dimensional characterization of components and materials. The possibility of an in-depth investigation of multi-material specimens is equally important in medical and industrial applications. However, XCT encounters some limitations when high-density materials such as metals are included in the specimen, particularly in close proximity to materials of lower density. The polychromatic nature of X-ray anodes in laboratory XCT devices causes well known beam hardening artifacts, which deteriorate the reconstructed XCT image data. Polychromatic beam hardening also plays an important role for metal artefacts which appear as bright and dark streaks between high-density objects (streak artifacts) [1]. Furthermore, gradients of decreasing grey values towards the center of otherwise homogeneous objects can appear (cupping artefacts).

Both streak and cupping artefacts are caused by the polychromatic X-ray spectrum which is not thoroughly considered in standard filtered backprojection (FBP) reconstruction algorithms. These algorithms are based on Lambert–Beer's law which implies a linear relationship between X-ray attenuation and specimen thickness and is strictly valid only for

✉ J. Glinz
jonathan.glinz@fh-wels.at

1 Institut Für Werkstoffwissenschaft Und Werkstofftechnologie, TU Wien, Getreidemarkt 9, 1060 Wien, Austria

2 Research Group Computed Tomography, University of Applied Sciences Upper Austria, Stelzhamerstraße 23, 4600 Wels, Austria

3 Lehrstuhl Für Röntgenmikroskopie, Universität Würzburg, Josef-Martin-Weg 63, 97074 Würzburg, Germany

4 Magnetic Resonance and X-Ray Department, Fraunhofer EZRT, Josef-Martin-Weg 63, 97074 Würzburg, Germany

monochromatic X-rays [2]. In a polychromatic spectrum, lower energy X-ray photons are attenuated more significantly. When beam hardening occurs, the X-ray spectrum is shifted to a higher mean energy while propagating through a specimen which results in a higher transmission as would be assumed from Lambert–Beer's law [3]. The resulting dark streaks between and around highly attenuating structures which are embedded in "softer" matrices usually appear in combination with bright ones as a result from high pass filtering in FBP reconstruction algorithms amplifying differences between adjacent pixels [4].

These streak artifacts are commonly encountered in XCT images of multi-material components, where they overlap with specimen features thereby hindering a proper materials segmentation by thresholding. Examples for metal artifacts in multi-material components like electrical plugs and circuit boards are shown in [5] and [6]. In medical imaging, these artifacts can greatly reduce the diagnostic value of XCT images and complicate the clinical reporting [7–9]. Typical scenarios of severe beam hardening occur in the monitoring of metal implants, e.g. after bone fracture. Meyer et al. [10] show cases of severe streak artifacts in patients with metallic hip prostheses, dental fillings and spine fixture. For these reasons, procedures to reduce beam hardening artifacts are a heavily addressed topic in medical imaging [3] and a considerable amount of scientific publications focus on their comparison [2, 7, 11–18]. However, phase contrast imaging (PCI) XCT, which is known to be less prone to metal artifacts caused by beam hardening effects [19, 20], has not yet been considered in these studies. In the course of this work, this absence in literature shall be addressed by a quantitative comparison of PCI to attenuation contrast (AC) XCT methods.

There are several techniques for the extraction of X-ray PCI explained in literature, such as analyzer crystal, propagation or edge illumination based methods [21]. In this work, we facilitate PCI by Talbot-Lau grating interferometer XCT (TLGI-XCT) [22]. In contrast to the majority of other methods, TLGI-XCT has rather low requirements in spatial and temporal coherence and is therefore applicable at most laboratory XCT devices with standard X-ray tubes [19]. As explained and demonstrated by Chabior et al. [19], beam hardening effects in PCI-XCT are qualitatively comparable to artifacts arising in AC-XCT. However, quantitatively, beam hardening artifacts are less pronounced because of a reduced dependency of X-ray refraction on X-ray energy. The linear attenuation coefficient μ is proportional to $\mu \sim 1/E^3$, while its equivalent in PCI $(2\pi/\lambda) \cdot \delta \sim 1/E$, where λ is the X-ray wavelength and δ the real refractive index decrement [19]. The dependency of attenuation and refraction on X-ray energy can also be expressed in terms of phase cross section σ_p and attenuation cross section σ_a. Figure 1 shows a comparison of σ_p and σ_a for titanium and carbon from 10 to 150 keV X-ray energy, in which the higher linearity of σ_p compared to σ_a is visible. Additionally, σ_p is up to three orders of magnitude higher than σ_a, which can result in better contrast-to-noise ratio (CNR) in PCI as shown by Zanette et al. [23] and Herzen et al. [24]. Because of this, PCI is most often used for the investigation of low density materials such as biological tissue [25] or polymers [26, 27]. Values for σ_p are calculated according to

$$\sigma_p = r_0 \lambda Z \tag{1}$$

where r_0 is the classical electron radius, the X-ray wavelength λ and the atomic number Z of the respective material [28].

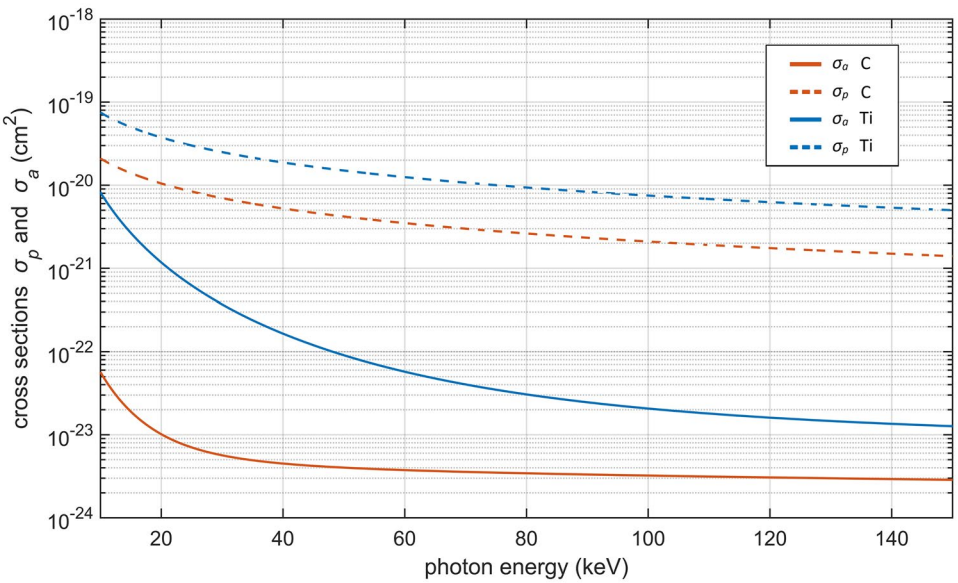

Fig. 1 Attenuation σ_a and phase cross section σ_p for titanium and carbon at X-ray energy from 10 to 150 keV. σ_p values were calculated according to equation (1) and σ_a values were obtained from XOP database [25]

Equation (1) is valid for X-ray energies far from absorption edges of the material. Values for σ_a are obtained from tabulated data in the XOP database software [29]. Further effects which contribute to a lower sensitivity of PCI-XCT to beam hardening effects are its reduced dependence on the actual signal intensity measured by the detector, and that in PCI using grating interferometry only a band of the X-ray energy spectrum, around the design energy of the interferometer, effectively contributes to the recorded phase image [30]. Gusenbauer et al. [31] have previously shown that PCI is capable to reduce metal artifacts in a carbon-fiber-reinforced polymer component including copper wires for lightning protection. Furthermore, Donath et al. [30] show a medical example of beam hardening artifact reduction by PCI.

In AC-XCT, one of the most commonly applied beam-hardening correction (BHC) methods is the pre-filtering of the X-ray beam with metallic plates (e.g. Al, Cu or Sn) which have 25%-50% of the objects attenuation length and remove low energy photons from the spectrum. Thereby, a harder energy spectrum is created at the expense of photon flux which generally contributes to a reduction of patient dose and beam hardening artifacts while slightly increasing the measurement time. I.e., the application of attenuation filters reduces photon statistics, leading to worse signal-to-noise ratios.

Another technique for the reduction of beam hardening effects which has been established particularly in medical imaging, is dual-energy XCT (DECT). At DECT, two images representing different energy spectra are recorded for every projection view and subsequently superimposed prior to XCT reconstruction. For most standard laboratory XCT devices this means two consecutive measurements at different acceleration voltages are required, which effectively at least doubles the measurement time. In medical XCT, dual source devices for the simultaneous acquisition of both energy channels are more commonly encountered. When the two different spectra are known, virtual monochromatic XCT images can be directly reconstructed from the dual projection data using an iterative reconstruction scheme. When applied at sufficiently high energy levels, these virtual monochromatic XCT images can reduce beam hardening artifacts significantly [4, 11]. However, consequently and contrary to PCI, contrast for low absorbing structures is reduced as well [11].

Besides DECT and attenuation-filtering digital metal artifact reduction (MAR) algorithms are commonly used due to their versatility and applicability on existing data. Consequently, many manufacturers of XCT systems already supply their devices with beam hardening correction methods, e.g. for the reduction of cupping effects, by default. MAR algorithms can be roughly categorized into physical effects correction (e.g. beam hardening, scatter, photon starvation), projection completion (interpolation) in the sinogram domain [32] and iterative reconstruction methods [33, 34]. However, hybrid forms combining different techniques have been developed as well [3]. Among these, the normalized MAR (NMAR) [10] was established as a state-of-the-art method [12, 34, 35]. Furthermore, MAR by deep learning methods gain increasing importance as computational power becomes more readily available with technological progress [34–36]. Comparative studies of different MAR algorithms for industrial [12] and medical applications [16, 37] can be found in literature. However, this work will extend literature by the quantitative comparison of PCI- to AC-XCT in combination with different hardware pre-filters and a MAR algorithm.

Materials and Methods

Specimen Design

For the investigation of beam hardening effects on image quality we designed a phantom specimen consisting of Polyamide 12 (PA12) including four Ti6Al4V inserts. The PA12 box of roughly 12×12×25 mm size was additively manufactured by selective laser sintering on an EOS P 396 device (EOS GmbH, Germany). The Ti6Al4V inserts of 1 mm diameter each were manufactured by selective laser melting on a Concept Laser M2 Cusing device (Concept Laser GmbH, Germany). The two components can be easily assembled and disassembled allowing measurements with and without metal parts in the specimen. A schematic image of the specimen can be seen in Fig. 2.

Experimental Setup and Parameters

Phase contrast measurements were performed on a SkyScan 1294 desktop device (Bruker microCT N.V., Belgium) which is a dedicated phase contrast system equipped with a Talbot-Lau grating interferometer formed by two absorption and one phase grating, with periods of 4.8 µm each, positioned in a symmetric setup. As the system was developed for a design energy of 30 keV, the maximum applicable acceleration voltage is limited to 50 kV. Additionally, a 0.045 mm thin copper pre-filter was applied to adjust the energy spectrum for the interferometry setup. For the measurement of titanium components this voltage is still rather low. However, a minimum transmission of roughly 7.5% was achievable. With a 4000×2672 pixel CCD camera in 2×2 binning mode the applicable voxel size of this system is fixed to 11.4 µm. Phase contrast images were extracted by a phase stepping procedure [38] in 4 steps over one grating period. As this effectively means a quadruplication of the acquisition time for each angular projection image, less projections and averaging were applied for PCI in order to reduce the total

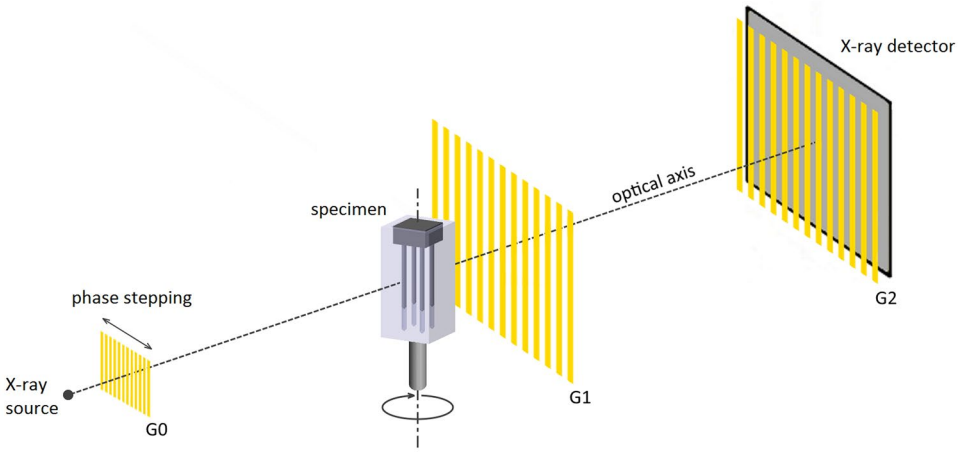

Fig. 2 Schematic grating interferometer setup of the SkyScan 1294 device used for phase contrast imaging. The specimen in the beam path as well as source- (G0), phase- (G1), and analyzer grating (G2) positions are indicated

scan time to approximately 3 h. Furthermore, to avoid grating misalignments caused by temperature drifts during the scans, the X-ray tube was conditioned for approximately 2 h prior to every scan. A voxel size calibration phantom (2 ruby ball bars, distance from sphere to sphere: 12 mm) was used for the calibration of voxel size in x–y and z direction.

Due to the low applicable voltage, the loss in photon flux caused by the interferometer gratings and the required phase stepping procedure, the SkyScan device is not particularly suited for standard AC measurements. Consequently, AC-XCT measurements were performed on a Nanotom 180NF (GE Sensing & Inspection Technologies GmbH, Germany) device for comparability. Two different parameter settings at 100 kV and 150 kV were used to investigate the effects of acceleration voltage in combination with varying pre-filter thickness on image quality. Furthermore, a reference scan of the PA12 box without titanium inserts was performed at a reduced acceleration voltage of 80 kV, to optimize image contrast. To allow for higher X-ray energies, a tungsten transmission target on diamond substrate was used in combination with a 2304×2304 pixel flat panel detector (Hamamatsu Photonics K.K., Japan). At the given specimen dimensions, a maximum resolution of 8 µm was achieved. The voxel size was calibrated by scanning of a commercially available ruby ball bar with 8 mm sphere distance. For comparability, measurement times were kept at approximately 3 h for all measurements. Detailed parameters are listed in Table 1.

Image Processing and Visualization

For comparability, all data sets have been reconstructed with the software X-AID (MITOS GmbH, Germany, version 2021.2.0, www.x-aid.de) by means of a filtered back-projection algorithm, which includes a feature for cupping and streaking artifact correction. The streak artifact correction method is based on an advanced NMAR algorithm and allows for an interactive reduction of streaks between and around high attenuating metal parts. Attenuation CT data was reconstructed with and without streaking correction for reference. Streak artifact correction parameters were determined empirically to minimize artifacts while avoiding overcorrection. No artifact correction was applied for PCI data. Reconstructed data was visualized in Volume Graphics Studio 3.4 (Volume Graphics GmbH, Germany) and aligned by a best fit algorithm.

Image Quality Metrics

For the quantification of streaking artifacts, we used a metric introduced by Cao et al. [39] which calculates the streak index (SI) on the basis of line profiles between two metal inserts as shown in Fig. 3. The equation defined by Cao et al. is as follows:

Table 1 Scanning parameters for attenuation- and TLGI-XCT

XCT-System	Voxel size µm	Voltage kV	Current µA	Exposure time ms	Projections	Averaging	Pre-filter mm	Time min
Nanotom 180 NF	8	100	120	500	2800	6	-	168
Nanotom 180 NF	8	150	150	800	2800	6	0.5 Cu	192
Skyscan 1294	11.4	50	1000	800	800	3	0.045 Cu	194
Nanotom 180 NF*	8	80	270	500	2800	6	-	168

*Parameters of the reference scan without titanium inserts

$$SI = \frac{1}{n} \times \sum_{i=1}^{n} \left(\frac{I_{ai} - I_{bi}}{\max\left(I_{ai}, I_{bi}\right) - M_b + C} \right) \tag{2}$$

where

$$I_a = \frac{I_{p1} + I_{p2}}{2} \tag{3}$$

and

$$I_b = \frac{I_{v1} + I_{v2}}{2} \tag{4}$$

However, equation (2) was slightly altered as it is designed for integer type datasets. As we were using floating comma point data for this work, the constant C, which keeps the SI in a range below 1, can be omitted. M_b is defined as the mean grey value in the image background (air) from a region not affected by streak artefacts. $I_{p1,2}$ and $I_{v1,2}$ are the line profile maxima and minima respectively, determined in the uncorrected dataset as shown in Fig. 3. Their positions in the line profile are used for the extraction of grey values in all following datasets. In the case of an overcorrection, the SI can reach negative values while (with the omission of C) a value above 1 indicates streak artifacts darker than the background grey value. From each data set, 60 line profiles were extracted from pore free regions and evaluated as explained above.

In order to compare the overall image quality and possible effects of MAR, the CNR was calculated subsequently according to [24]:

$$CNR = \frac{|\mu_m - \mu_b|}{\sqrt{\sigma_m^2 + \sigma_b^2}} \tag{5}$$

where μ_m and μ_b are the mean signals and σ_m and σ_b their standard deviations measured in the material and background (air) respectively. Material values were extracted from the whole cross section of the PA12 box excluding pores and titanium inserts. Pores and drill holes for titanium inserts were determined via a reference scan of the PA12 box without titanium inserts and subtracted from the cross-sections. For every dataset, CNR values were extracted in a region affected by streak artefacts and in an artefact free region below the height of the metal inserts for comparison.

Results

Reconstructed slice images of the specimen resulting from different beam hardening correction methods are shown in Fig. 4. Without the application of a pre-filter to remove low energy photons from the spectrum, severe streak artifacts emerge between and around the metal inserts (Fig. 4(a)) in AC-XCT. The streak artifacts cover potentially interesting structures in the lower attenuating polymer and, e.g., evaluation of porosity will be heavily affected. Also, with the application of a MAR algorithm, these artifacts are too severe to be completely removed by post-processing of the data (Fig. 4(b)). By application of a 0.5 mm copper pre-filter, streak artifacts can be significantly reduced, but not completely avoided as shown in Fig. 4(c). Though, with subsequent application of a MAR algorithm, a streak index close to zero can be achieved without significant overcorrection (Fig. 4(d)). In PCI-XCT streak artifacts are perceptibly lower. However, because of the high refraction of X-rays caused at the metal inserts, additional streaks in radial direction of the inserts arise because of phase wrapping effects [23]. Furthermore, when comparing PCI and AC slice images, the metal inserts appear to be larger in AC, because of their much higher attenuation in reference to the surrounding polymer. Consequently, the metal appears to be radiating across its actual material borders, which complicates the visualization of structures in close proximity to the metal inserts.

In Fig. 5, boxplots of the streak index for 60 line profiles in each dataset are shown. The mean streak index according to equation (2) is indicated with a cross (x) and outliers with a plus (+) symbol. The biggest improvement in SI by MAR algorithm can be observed in the AC dataset without pre-filtering applied, reducing it to a similar level as for the AC dataset with 0.5 mm copper pre-filter, but without MAR algorithm applied. This pre-filtered AC dataset can further

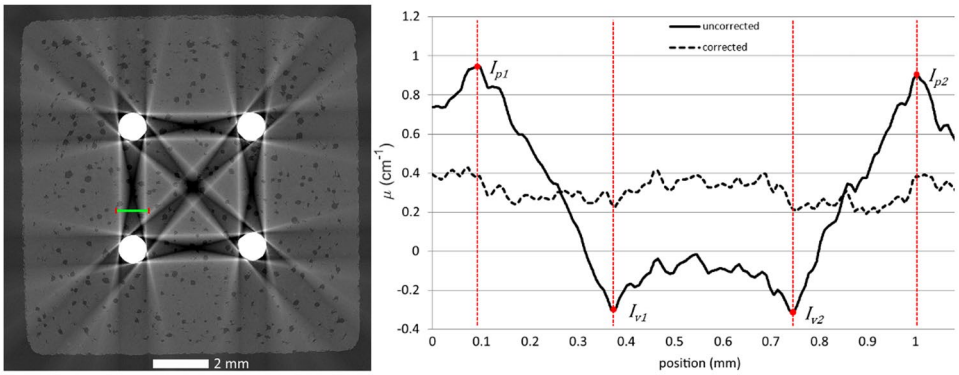

Fig. 3 Line profile across a streak artifact as indicated in the cross-section (green line) on the left. Maxima and minima (Ip1,2 and Iv1,2) detected in the uncorrected dataset are shown in comparison to the same line profile from a dataset corrected using a MAR algorithm

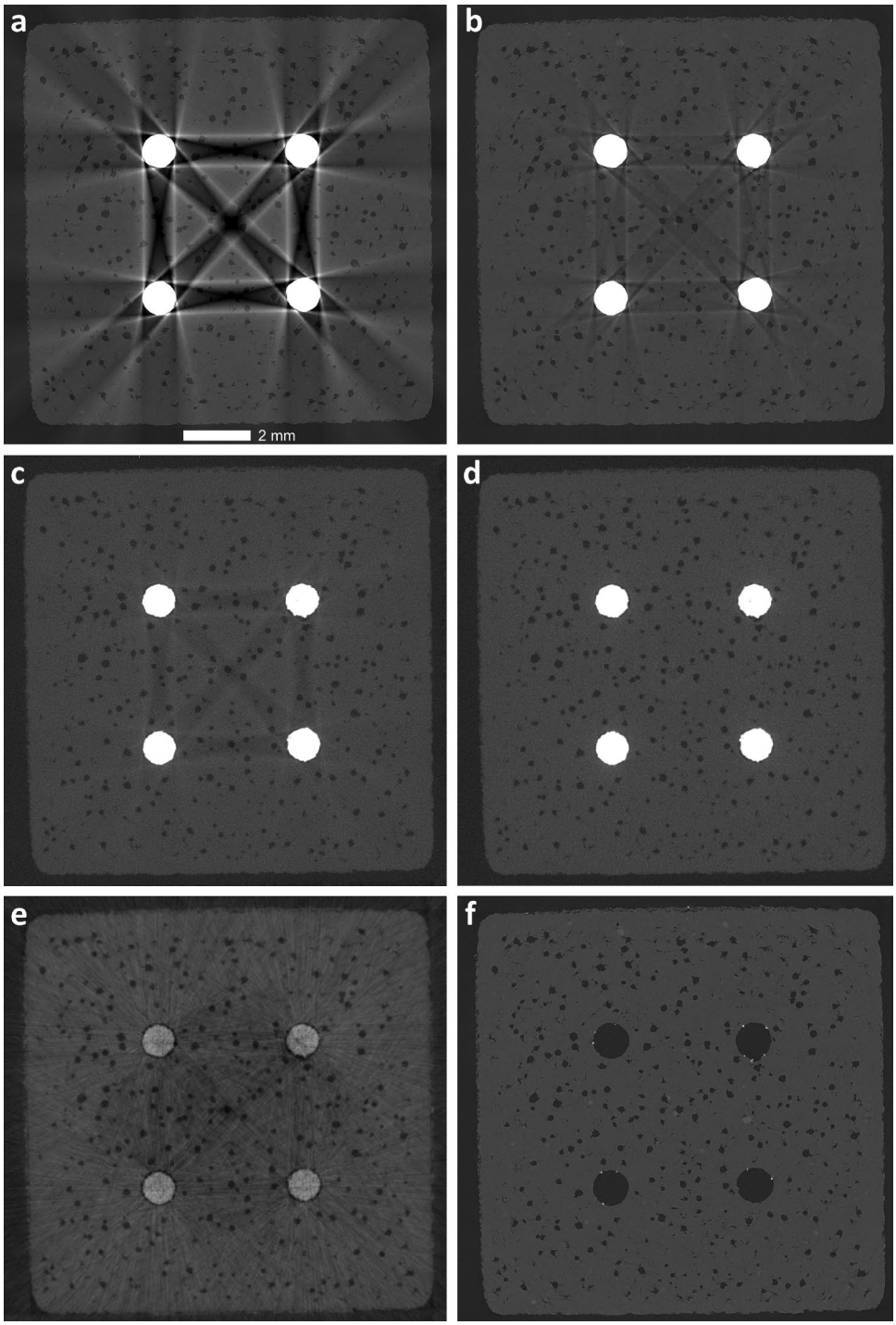

Fig. 4 Cross-sectional images of the specimen. (**a**) AC-XCT without pre-filter, without MAR. (**b**) AC-XCT without pre-filter, with MAR. (**c**) AC-XCT with 0.5 mm Cu pre-filter, without MAR (**d**) AC-XCT with 0.5 mm Cu pre-filter, with MAR. (**e**) PCI-XCT (**f**) AC-XCT reference scan without metal inserts. In PCI-XCT, additional streak artifacts emerging radial from the metal inserts (caused by phase wrapping) are visible

be corrected to a SI close to zero, while the SI of the PCI dataset levels somewhere midrange between MAR corrected and uncorrected pre-filtered AC data. As a reference, the SI in a dataset without metal inserts is plotted as well, which is slightly below zero, because of image noise.

For the investigation of edge sharpness and the effects of metal artifacts on the detectability of material interfaces, additional line profiles across two pores as well as one metal insert are shown in Fig. 6. Line profiles were plotted for both datasets with MAR algorithms applied, the PCI-XCT dataset and the dataset without metal inserts. A lower edge sharpness in PCI-XCT due to the reduced spatial resolution caused by the extended source size of the SkyScan system [40] can be seen by the reduced slope at pore interfaces. Additional edge enhancement in attenuation XCT data, caused by propagation based phase effects, is visible in some

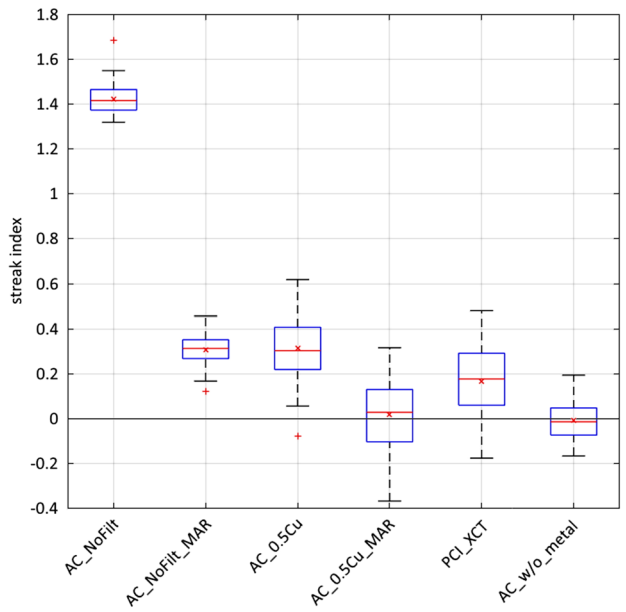

Fig. 5 Streak index boxplots for all datasets investigated. From left to right: AC-XCT without pre-filter, without MAR. AC-XCT without pre-filter, with MAR. AC-XCT with 0.5 mm Cu pre-filter, without MAR. AC-XCT with 0.5 mm Cu pre-filter, with MAR. PCI-XCT. AC-XCT without metal inserts. The mean streak index is indicated by a cross (x), outliers with a plus (+) symbol

cases. The low CNR in pre-filtered data is also clearly visible as well as declining grey values towards the center of the specimen in PCI. When comparing line profiles across the metal insert in AC and PCI, it becomes more obvious, that artifacts close to the metal surface overlap a gap between the metal insert and polymer box in AC. In PCI-XCT, such a gap is clearly visible in both the cross-section image and line profile. Mean grey values of the polymer material are indicated with dashed horizontal lines to highlight the increased grey values around the metal insert in AC.

CNRs in regions with and without streak artifacts are shown in Fig. 7. In regions without streak artifacts, unfiltered as well as PCI-XCT data show CNRs comparable to the reference measurement without metal inserts. However, in regions with streak artifacts, CNR is greatly reduced. Therefore, in unfiltered datasets, a significant part of CNR can be regained by application of artifact correction algorithms. Hardware pre-filtering on the other hand clearly reduces the CNR as a consequence of the reduction in photon count. Additionally, due to the higher acceleration voltage applied, increased photon energies lead to a reduction of the linear attenuation coefficient μ, which further reduces the CNR. Consequently, streak artifacts decrease the already low CNR only marginally as well as MAR algorithms have only minor effect on it. The CNR of PCI-XCT data positions on second place in the comparison. The consistent CNR in regions without streak artifacts before and after MAR algorithms were applied indicates that the applied algorithm affects only regions where actual streak artifacts are present. SI and CNR values evaluated are listed in Table 2.

Discussion

The comparison of five datasets with different streak artifact reduction approaches shows how significantly different contrast modalities can affect the resulting image quality. Besides well-established methods, such as hardware pre-filtering of the X-ray spectrum, we have shown that the reduced sensitivity of PCI-XCT to beam hardening effects can provide an alternative modality for investigations e.g. of multi material components. However, it is clear that PCI-XCT comes with its own limitations and problems when investigating multi material components including metal parts. As could be seen in Fig. 4(e), additional streak artifacts appearing in radial direction from the metal inserts can deteriorate image quality and also affect the CNR. Zanette et al. [23] found that such artifacts are entirely caused by phase wrapping effects whereas Massimi et al. [41] presented an artifact reduction algorithm significantly reducing these streaks recently. Moreover, a gradient towards lower grey values in the center of the specimen, between the metal inserts, can be observed. The reason for this lies in the X-ray energy dependent efficiency of the interferometer [30, 42]. Particularly the metal inserts cause a hardening of the X-ray spectrum and therefore a mismatch with the design energy of the grating interferometer. Consequently, a segmentation of the polymer material volume, e.g. by global threshold, is impeded. However, this effect can also be reduced by use of a more appropriate interferometer setup. The grating interferometer used for this work was not particularly designed for investigations including metal components, as its design energy lies at 30 keV with a maximum applicable peak energy of 50 keV. Using current state of the art interferometer gratings, significantly higher design and peak energies can be realized, which will positively affect beam hardening as well as measurement time can be reduced. Also, additional MAR methods for PCI-XCT may be developed, e.g. as shown by Yan et al. [43], who introduced a MAR method applicable for inhomogeneous, multi-material specimens.

The resulting SI in Fig. 5 showed that, in terms of streak artifacts, PCI-XCT is superior to AC-XCT when no MAR algorithms are applied. Nonetheless, larger, high density metallic components might still push PCI-XCT to its limits. The use of AC imaging in combination with pre-filters and/or MAR algorithms therefore is equally valid. Although, often a compromise between image noise and streak artifact reduction has to be made when hardware pre-filters are applied. In case of the specimen investigated, streak artifacts could not be completely removed by the MAR algorithm if

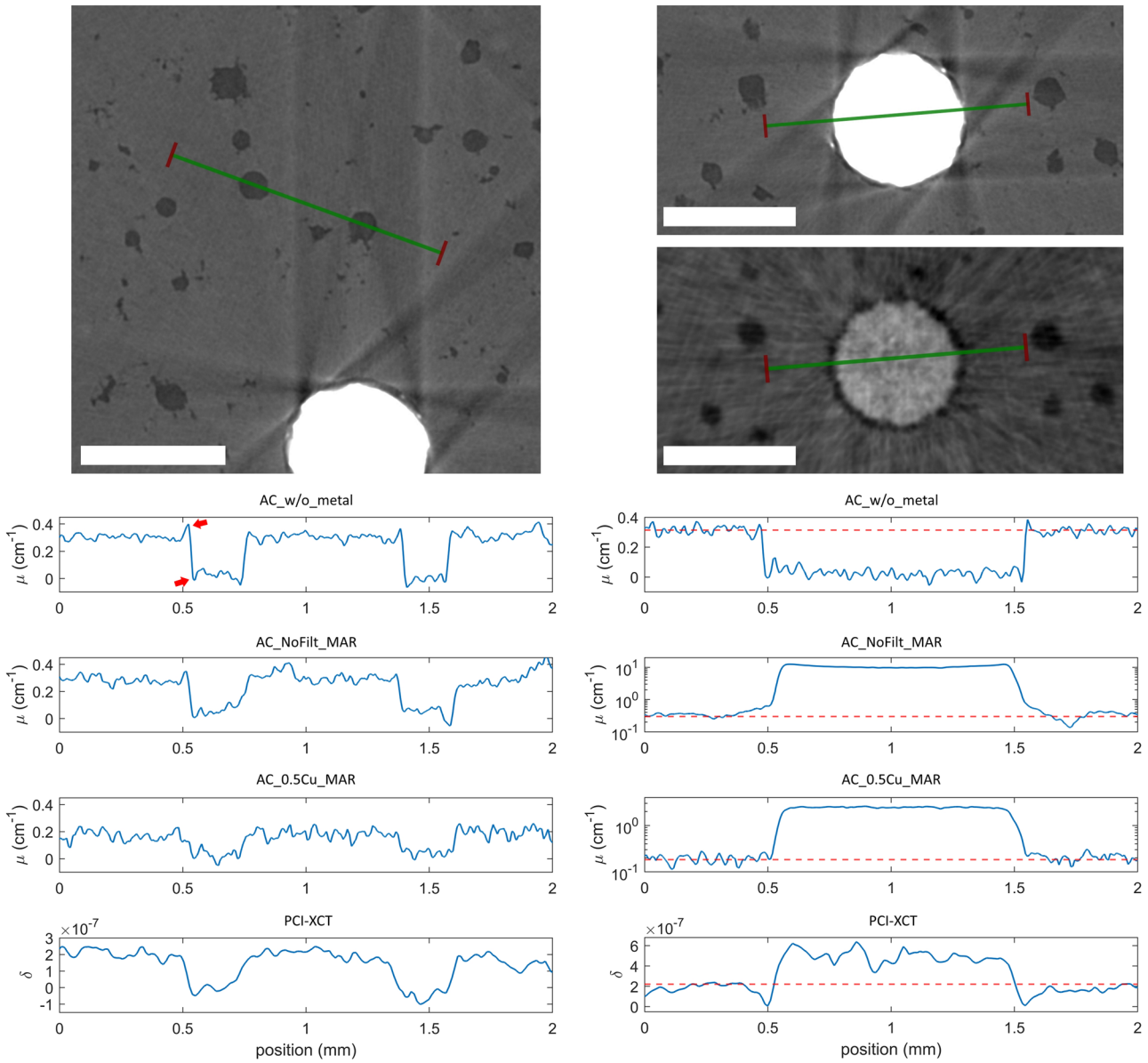

Fig. 6 Line profiles through two pores on the left and through a metal insert on the right. Polymer material mean grey values are indicated by horizontal dashed lines. Red arrows indicate edge enhancement caused by propagation based phase effects in AC_w/o_metal. Note the logarithmic scale in some of the plots. Scale bars correspond to 1 mm

no pre-filter was used at all. With a pre-filter of 0.5 mm Cu applied the remaining artifacts could be removed by the MAR algorithm sufficiently enough to achieve a SI of zero at a considerably reduced CNR. Consequently, a reduction of the pre-filter, e.g. to 0.2 mm Cu, might be the most obvious solution, as long as remaining artifacts can still be removed by MAR algorithms.

These MAR algorithms proved to be efficient for simple geometries as shown in this work. However, increasing size and geometrical complexity of metal parts will often lead to less satisfying results. Moreover, MAR algorithms can also introduce new artifacts, e.g. by overcorrection, as experienced at various examples in literature [15, 37, 44]. We also found, that although streak artifacts distant from the metal inserts can be removed acceptably well, artifacts close to the metal surface still remain. This can hinder the inspection of the metal-polymer interface and gaps between the materials might be underestimated or thin gaps even completely missed. Also in medical applications, regions in close proximity to metal implants often are of particular interest for diagnostic reasons [8].

The evaluation of CNR in streak affected and streak free regions indicates that the MAR algorithm used during this work does affect only regions where streak artifacts occur.

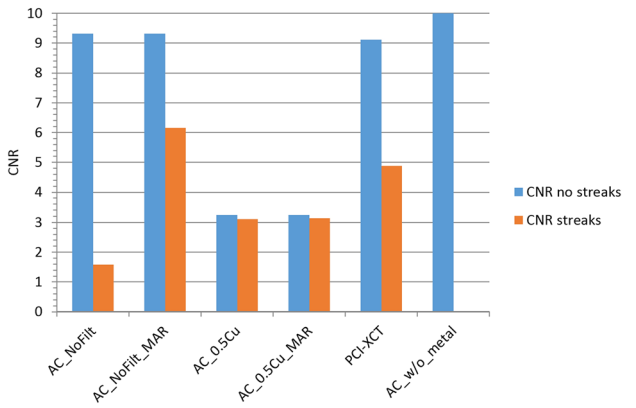

Fig. 7 Comparison of the CNR in all datasets investigated. Blue bars correspond to the CNR in regions unaffected by beam hardening artifacts. Orange bars correspond to the CNR in regions with beam hardening artifacts

In streak free regions, CNR is consistent before and after MAR. In case of the hardware pre-filtered datasets, CNR is mostly decreased by image noise and the reduced attenuation coefficient at high photon energies as the subsequent MAR has only little effect on it. On the contrary, datasets without pre-filtering show greatly increased CNR after the application of a MAR algorithm, indicating that the reduction in CNR is mostly caused by streak artifacts. The high CNR in PCI-XCT (being second only to the unfiltered but metal artifact corrected dataset) was previously also experimentally investigated by Zanette et al. [23] and Herzen et al. [24]. Furthermore, streak artifacts from phase wrapping effects as well as more pronounced ring artifacts most likely caused an additional reduction of CNR in the PCI-XCT dataset. Consequently, CNR could be enhanced significantly if respective artifact reduction methods are applied. However, the main focus of this work was the investigation of the influence of metal artifacts and artifact reduction methods on the CNR for which the uncorrected datasets are considered sufficient. For sake of comparability, parameters of individual measurements were chosen to achieve measurement times of approximately three hours. Nevertheless, PCI and pre-filtered AC scans took up to 26 min longer. Consequently, AC scans without pre-filtering might actually result in slightly better CNR values than depicted in Fig. 7.

Table 2 Streak index (SI) and contrast-to-noise ratio (CNR) evaluated in regions with and without streak artifacts of every dataset investigated

	SI	CNR no streaks	CNR streaks
AC_NoFilt	1.422 ± 0.066	9.315	1.582
AC_NoFilt_MAR	0.305 ± 0.066	9.315	6.157
AC_0.5Cu	0.313 ± 0.132	3.244	3.107
AC_0.5Cu_MAR	0.018 ± 0.161	3.244	3.131
PCI-XCT	0.167 ± 0.164	9.110	4.887
AC_w/o_metal	-0.008 ± 0.078	10.157	-

Conclusions

We have shown that the reduced sensitivity of PCI-XCT to beam hardening effects can improve streak artifacts in multi-material components. We presented the first quantitative comparison of PCI-XCT which has been widely neglected in comparative studies of MAR methods so far. Furthermore, PCI-XCT showed relatively high CNR while hardware pre-filtering in combination with MAR algorithms often requires a compromise between CNR and effective artifact reduction. However, PCI-XCT also comes with its own limitations such as relatively low spatial resolution and artifacts caused by phase wrapping. Most other drawbacks typically found in literature can widely be counteracted by use of appropriate phase contrast method and system design. To this end, PCI offers a lot of potential for industrial as well as medical applications. Future investigations will include the application to a selection of use-cases such as electronic devices or medical implants like bone fixations and artery stents.

Funding Open access funding provided by University of Applied Sciences Upper Austria. This work was financed by the project "PhadCT" funded by the federal government of Upper Austria [FFG grant number: 875432], and the project "SpaceNDT" funded by the federal ministry for climate action, environment, energy, mobility, innovation and technology and the Austrian Space Applications Programme [FFG grant number: 866013].

Declarations

Conflict of Interests The authors declare that they have no known competing financial interests or personal relationships that could have appeared to influence the work reported in this paper.

References

1. Kastner J, Heinzl C (2019) X-ray tomography. In: Ida N, Meyendorf N (eds) Handbook of Advanced Nondestructive Evaluation. Springer, Cham, pp 1095–1166

2. Van de Casteele E (2004) Model-based approach for beam hardening correction and resolution measurements in microtomography. University of Antwerp, Belgium, pp 1–142 (PhD thesis)
3. Gjesteby L, De Man B, Jin Y et al (2016) Metal Artifact Reduction in CT: Where Are We After Four Decades? IEEE Access 4:5826–5849. https://doi.org/10.1109/ACCESS.2016.2608621
4. Boas FE, Fleischmann D (2012) CT artifacts: causes and reduction techniques. Imaging Med 4:229–240
5. Maier J (2019) Artifact Correction and Real-Time Scatter Estimation for X-Ray Computed Tomography in Industrial Metrology. Ruperto-Carola University, Heidelberg, pp 1–171. https://doi.org/10.11588/heidok.00026701 (PhD thesis)
6. Kano T, Koseki M (2017) Development of a multi-axis X-ray CT for highly accurate inspection of electronic devices. In: 7th Conference on Industrial Computed Tomography. Leuven, pp 1–7
7. Huang JY, Kerns JR, Nute JL et al (2015) An evaluation of three commercially available metal artifact reduction methods for CT imaging. Phys Med Biol 60:1047–1067. https://doi.org/10.1088/0031-9155/60/3/1047
8. Barrett JF, Keat N (2004) Artifacts in CT: Recognition and Avoidance. Radiographics 24:1679–1691. https://doi.org/10.1148/rg.246045065
9. Trieb K, Glinz J, Reiter M et al (2019) Non-Destructive Testing of Ceramic Knee Implants Using Micro-Computed Tomography. J Arthroplasty 34:2111–2117. https://doi.org/10.1016/j.arth.2019.05.006
10. Meyer E, Raupach R, Lell M et al (2010) Normalized metal artifact reduction (NMAR) in computed tomography. Med Phys 37:5482–5493. https://doi.org/10.1118/1.3484090
11. Katsura M, Sato J, Akahane M et al (2018) Current and novel techniques for metal artifact reduction at CT: Practical guide for radiologists. Radiographics 38:450–461. https://doi.org/10.1148/rg.2018170102
12. Gusenbauer C, Reiter M, Salaberger D, Kastner J (2016) Comparison of Metal Artefact Reduction Algorithms from Medicine Applied to Industrial XCT Applications. In: 19th World Conference on Non-Destructive Testing. Munich, pp 1–9
13. Diehn FE, Michalak GJ, DeLone DR et al (2017) CT Dental Artifact: Comparison of an Iterative Metal Artifact Reduction Technique with Weighted Filtered Back-Projection. Acta Radiol Open 6:1–8. https://doi.org/10.1177/2058460117743279
14. Joemai RMS, De Bruin PW, Veldkamp WJH, Geleijns J (2012) Metal artifact reduction for CT: Development, implementation, and clinical comparison of a generic and a scanner-specific technique. Med Phys 39:1125–1132. https://doi.org/10.1118/1.3679863
15. De Crop A, Casselman J, Van Hoof T et al (2015) Analysis of metal artifact reduction tools for dental hardware in CT scans of the oral cavity: kVp, iterative reconstruction, dual-energy CT, metal artifact reduction software: does it make a difference? Neuroradiology 57:841–849. https://doi.org/10.1007/s00234-015-1537-1
16. Wagenaar D, Van Der Graaf ER, Van Der Schaaf A, Greuter MJW (2015) Quantitative comparison of commercial and non-commercial metal artifact reduction techniques in computed tomography. PLoS ONE 10:1–9. https://doi.org/10.1371/journal.pone.0127932
17. Reiter M, de Oliveira FB, Bartscher M et al (2019) Case Study of Empirical Beam Hardening Correction Methods for Dimensional X-ray Computed Tomography Using a Dedicated Multi-material Reference Standard. J Nondestruct Eval 38:1–15. https://doi.org/10.1007/s10921-018-0548-3
18. Rodríguez-Gallo Y, Orozco-Morales R, Pérez-Díaz M (2021) Inpainting-filtering for metal artifact reduction (IMIF-MAR) in computed tomography. Phys Eng Sci Med 44:409–423. https://doi.org/10.1007/s13246-021-00990-8
19. Chabior M, Donath T, David C et al (2011) Beam hardening effects in grating-based x-ray phase-contrast imaging. Med Phys 38:1189–1195. https://doi.org/10.1118/1.3553408
20. Bevins N, Zambelli J, Li K et al (2011) Beam hardening in x-ray differential phase contrast computed tomography. In: Proceedings of the SPIE, pp 1–6
21. Endrizzi M (2018) X-ray phase-contrast imaging. Nucl Instruments Methods Phys Res Sect A Accel Spectrometers. Detect Assoc Equip 878:88–98. https://doi.org/10.1016/j.nima.2017.07.036
22. Pfeiffer F, Weitkamp T, Bunk O, David C (2006) Phase retrieval and differential phase-contrast imaging with low-brilliance X-ray sources. Nat Phys 2:258–261. https://doi.org/10.1038/nphys265
23. Zanette I, Weitkamp T, Lang S et al (2011) Quantitative phase and absorption tomography with an X-ray grating interferometer and synchrotron radiation. Phys Status Solidi Appl Mater Sci 208:2526–2532. https://doi.org/10.1002/pssa.201184276
24. Herzen J, Donath T, Pfeiffer F et al (2009) Quantitative phase-contrast tomography of a liquid phantom using a conventional x-ray tube source. Opt Express 17:10010–10018. https://doi.org/10.1364/oe.17.010010
25. Olivo A, Gkoumas S, Endrizzi M et al (2013) Low-dose phase contrast mammography with conventional x-ray sources. Med Phys 40:1–6. https://doi.org/10.1118/1.4817480
26. Gusenbauer C, Leiss-Holzinger E, Senck S et al (2016) Characterization of medical and biological samples with a Talbot-Lau grating interferometer µXCT in comparison to reference methods. Case Stud Nondestruct Test Eval 6:30–38. https://doi.org/10.1016/j.csndt.2016.02.001
27. Glinz J, Šleichrt J, Kytýř D et al (2021) Phase-contrast and dark-field imaging for the inspection of resin-rich areas and fiber orientation in non-crimp vacuum infusion carbon-fiber-reinforced polymers. J Mater Sci 56:9712–9727. https://doi.org/10.1007/s10853-021-05907-0
28. Zanette I (2011) Interférométrie X à réseaux pour l'imagerie et l'analyse de front d'ondes au synchrotron. Université Grenoble Alpes, France, pp 1–201 (PhD thesis)
29. Sanchez del Rio M, Dejus RJ (2004) Status of XOP: an x-ray optics software toolkit. In: Proc. SPIE, Bellingham, pp 171–174
30. Donath T, Pfeiffer F, Bunk O et al (2010) Toward clinical X-ray phase-contrast CT: Demonstration of enhanced soft-tissue contrast in human specimen. Invest Radiol 45:445–452. https://doi.org/10.1097/RLI.0b013e3181e21866
31. Gusenbauer C, Reiter M, Plank B et al (2017) Multi-modal Talbot-Lau grating interferometer XCT data for the characterization of carbon fibre reinforced polymers with metal components. In: Proceedings of the 7th Conference on Industrial Computed Tomography, pp 1–9
32. Amirkhanov A, Heinzl C, Reiter M et al (2011) Projection-Based Metal-Artifact Reduction for Industrial 3D X-ray Computed Tomography. IEEE Trans Vis Comput Graph 17:2193–2202. https://doi.org/10.1109/TVCG.2011.228
33. Hsieh J, Molthen RC, Dawson CA, Johnson RH (2000) An iterative approach to the beam hardening correction in cone beam CT. Med Phys 27:23–29. https://doi.org/10.1118/1.598853
34. Zhang Y, Member S, Yu H, Member S (2018) Convolutional Neural Network Based Metal Artifact Reduction in X-Ray Computed Tomography. IEEE Trans Med Imaging 37:1370–1381. https://doi.org/10.1109/TMI.2018.2823083
35. Gjesteby L, Yang Q, Xi Y et al (2017) Reducing Metal Streak Artifacts in CT Images via Deep Learning: Pilot Results. In: The 14th International Meeting on Fully Three-Dimensional Image Reconstruction in Radiology and Nuclear Medicine, pp 611–614
36. Willemink MJ (2019) The evolution of image reconstruction for CT – from filtered back projection to artificial intelligence. Eur Radiol 29(5):2185–2195
37. Golden C, Mazin SR, Boas FE et al (2011) A comparison of four algorithms for metal artifact reduction in CT imaging. Med Imaging 2011 Phys Med Imaging 7961:841–852. https://doi.org/10.1117/12.878896

38. Weitkamp T, Diaz A, David C et al (2005) X-ray phase imaging with a grating interferometer. Opt Express 13:6296–6304. https://doi.org/10.1364/OPEX.13.006296
39. Cao W, Sun T, Fardell G et al (2018) Comparative performance assessment of beam hardening correction algorithms applied on simulated data sets. J Microsc 272:229–241. https://doi.org/10.1111/jmi.12746
40. Birnbacher L, Willner M, Velroyen A et al (2016) Experimental Realisation of High-sensitivity Laboratory X-ray Grating-based Phase-contrast Computed Tomography. Sci Rep 6:1–8. https://doi.org/10.1038/srep24022
41. Massimi L, Savvidis S, Endrizzi M, Olivo A (2021) Improved visualization of X-ray phase contrast volumetric data through artifact-free integrated differential images. Phys Medica 84:80–84. https://doi.org/10.1016/j.ejmp.2021.03.024
42. Yashiro W, Vagovič P, Momose A (2015) Effect of beam hardening on a visibility-contrast image obtained by X-ray grating interferometry. Opt Express 23:23462–23471. https://doi.org/10.1364/oe.23.023462
43. Yan A, Wu X, Liu H (2017) Beam hardening correction in polychromatic x-ray grating interferometry. Opt Express 25:24690–24704. https://doi.org/10.1364/oe.25.024690
44. Wayer DR, Kim NY, Otto BJ et al (2019) Unintended consequences: Review of new artifacts introduced by iterative reconstruction CT metal artifact reduction in spine imaging. Am J Neuroradiol 40:1973–1975. https://doi.org/10.3174/ajnr.A6238